UDK 621.89:531.43:546.26
Izvirni znanstveni članek

ISSN 1580-2949
MTAEC9, 37(1-2)9(2003)

INFLUENCE OF OIL ADDITIVES ON THE PERFORMANCE OF DLC COATINGS

VPLIV ADITIVOV NA TRIBOLOŠKE LASTNOSTI PREVLEK NA OSNOVI TRDEGA OGLJIKA

Bojan Podgornik[1], Staffan Jacobson[2], Sture Hogmark[2]

[1]Center za tribologijo in tehnično diagnostiko, Univerza v Ljubljani, Bogišičeva 8, SI-1000 Ljubljana, Slovenija
[2]The Tribomaterials Group, Ångström Laboratory, Uppsala University, Box 534, SE-751 21 Uppsala, Sweden
bojan.podgornik@ctd.uni-lj.si

Prejem rokopisa - received: 2002-11-11; sprejem za objavo - accepted for publication: 2003-02-27

Hard coatings are becoming increasingly important in the field of machine components. Because they are able to improve the wear resistance and provide excellent frictional properties, diamond-like, hard carbon (DLC) coatings provide a great opportunity for improving the durability and reducing the frictional losses of machine components. However, the majority of machine components operate under lubricated conditions, where interactions between the surface and the lubricant play a significant role. Especially under boundary lubrication conditions, these interactions will determine the tribological behaviour of the contact. One of the main factors that limits the use of hard coatings in machine-component applications is the lack of knowledge relating to how these inert coatings perform under lubricated conditions with today's oils, which were originally designed for steel/steel contact situations.

The aim of this study was to investigate the influence of conventional extreme-pressure (EP) and anti-wear (AW) additives for gearbox oils on the tribological performance of DLC-coated steel surfaces in the boundary lubrication regime. The results of our investigation show that the introduction of DLC coatings can also significantly improve the tribological performance of a contact under boundary lubrication conditions.

Key words: boundary lubrication, additives, DLC coatings, friction

Trde prevleke se poleg odrezovalnih orodij vse bolj uveljavljajo tudi na področju strojnih elementov. Predvsem prevleke na osnovi trdega ogljika, ki imajo zelo dobro obrabno odpornost in nizek koeficient trenja proti različnim materialom, dajejo izjemne možnosti za izboljšanje obstojnosti ter zmanjšanje tornih izgub mehanskih sistemov. Po drugi strani pa večina mehanskih sistemov deluje v razmerah mazanega kontakta, kjer so interakcije med kontaktno površino in mazivom izredno pomembne. Še posebej v primeru mejnega mazanja je tribološko vedenje kontaktnih površin v največji meri odvisno od medsebojnega delovanja med mazivom in površino ter sposobnostjo tvorjenja mejnih mazalnih plasti. Prav pomanjkanje znanja o tribološkem vedenju inertnih trdih prevlek v kombinaciji z razpoložljivimi mazivi pa je ena od glavnih ovir za uspešno uporabo trdih prevlek v strojništvu.

Cilj predstavljene raziskave je bil raziskati vpliv konvencionalnih protiobrabnih aditivov (AW) in aditivov proti visokim tlakom (EP) za reduktorska olja na tribološko vedenje prevlek na osnovi trdega ogljika. Rezultati kažejo, da tudi v primeru mejnega mazanja nanos prevleke na osnovi trdega ogljika močno izboljša tribološke lastnosti kontaktnih površin.

Ključne besede: mejno mazanje, aditivi, DLC-prevleke, trenje

1 INTRODUCTION

Diamond coatings, diamond-like carbon (DLC) coatings and coatings with carbon-rich outer layers are hard and wear resistant. In addition, they also give low friction when in contact with different materials [1,2]. Therefore, by both improving the wear resistance and providing excellent frictional properties, hard, low-friction coatings provide a great opportunity to improve the durability and reduce the frictional losses of machine components [2-5]. However, the tribological properties of hard, low-friction coatings, especially DLC coatings, are greatly influenced by the surrounding environmental conditions [4,6]. The majority of machine components are operating under lubricated conditions, where interactions between the surface and the lubricant play a significant role. Especially under boundary lubrication conditions, chemical interactions between the oil additives, oxygen in the ambient atmosphere and the metallic surfaces will determine the tribological behaviour of the contact [7]. One of the main factors that limits the use of hard coatings in machine-component applications is the lack of knowledge relating to how these inert coatings perform under lubricated conditions with today's oils and additives, which were originally designed for steel/steel contact situations.

The aim of this study was to investigate the influence of conventional extreme-pressure (EP) and anti-wear (AW) additives on the tribological performance of hard, low-friction coatings in the boundary lubrication regime.

2 EXPERIMENTAL

WC-doped, hydrogenated, diamond-like carbon coatings with a multilayer structure of WC and C were used in this investigation. They were deposited in a reactive sputtering process with a deposition temperature of about 230 °C. The total coating thickness was about 2 μm, and its hardness about 1200 HV. The substrate

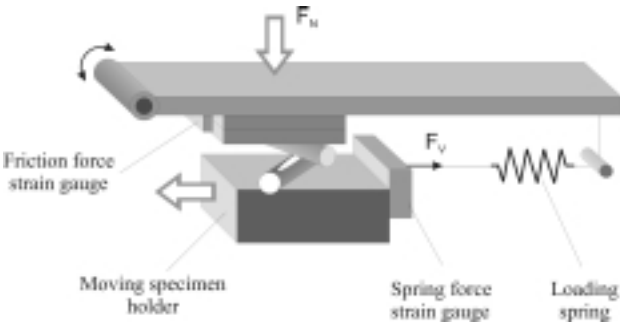

Figure 1: Load-scanning test rig
Slika 1: Shematičen prikaz naprave za preizkušanje

material used was high-speed tool steel (0.9%C, 4%Cr, 5%Mo, 1%V, 2%W, 2.5%Co) with a hardness of 850 HV and surface roughness, R_a, about 0.1 μm.

Boundary-lubricated friction and wear tests were performed in a load scanner. The special configuration of the test rig (**Figure 1**), involving two crossed, elongated cylinders (ϕ 10 mm), which are submerged in oil and forced to slide reciprocally against each other at a constant speed, allows the normal load to gradually increase during the forward stroke and to correspondingly decrease during the reverse stroke [8,9].

The sliding speed was fixed at 0.1 m/s, the range of the normal load was of the order of 140–1700 N, corresponding to 2.4–5.6 GPa contact pressure, and the largest number of test cycles was 30,000. The test oil was poly-alpha-olefin oil (PAO). This investigation included pure POA oil, PAO mixed with a commercial sulphur-based EP additive (PAO+EP) and PAO mixed with a zincdithiophosphate-based AW additive (PAO+AW).

3 RESULTS AND DISCUSSION

Figure 2 shows friction curves for a steel/steel combination at a normal load of 700 N. In the case of pure PAO oil the friction coefficient was reduced during the first 40 cycles from high initial values (~0.25) to values normally experienced under boundary lubrication conditions ($\mu \leq 0.1$). The use of additives reduced the number of initial high-friction cycles down to 10, followed by a steady-state friction of ~0.08, as shown in **Figure 2**.

Compared to the steel/steel combination, the application of DLC coatings in the boundary lubrication conditions reduced the initial high coefficient of friction to ~0.12 for the DLC/DLC combination, and even down to ~0.1 for the DLC/Steel. The use of additives had no effect on the friction behaviour of coated surfaces during the running-in process. However, when the number of cycles was further increased the additives had a pronounced effect, as shown in **Figure 3**. In the case of the pure PAO oil the DLC-coated surfaces showed a similar frictional behaviour to the uncoated surfaces with

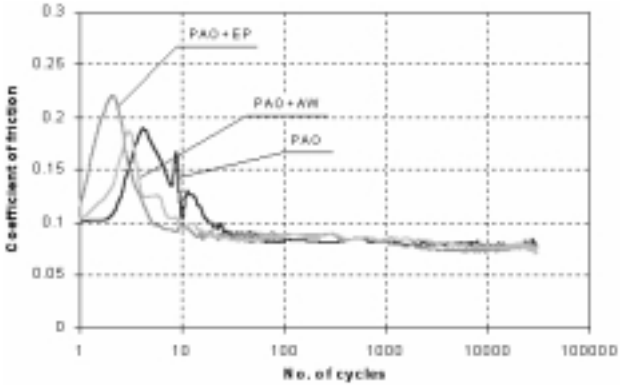

Figure 2: Friction curves for the steel/steel combination, recorded at 700 N load
Slika 2: Koeficient trenja za kombinacijo jeklo/jeklo; obremenitev 700 N

a steady-state coefficient of friction equal to ~0.08. Use of the EP-additive oil led to a reduction of the friction coefficient to 0.05-0.06 after the first 200-500 cycles. After about 4,000 cycles the friction coefficient started to increase again, reaching a value typical for a pure PAO oil (~0.08) at about 10,000 cycles, and maintaining this level until the end of the test, as shown in **Figure 3**. The AW-additive oil showed similar results, with the friction coefficient reaching a minimum value after 1,000–8,000 cycles, maintaining this value for a couple of thousand cycles, and again reaching 0.08 at the end of the test (**Figure 3**). Similar frictional behaviour was observed for the whole load range investigated.

The minimum value of the steady-state friction and the wear volume per unit length after 8,000 cycles, both corresponding to points along the contact subjected to a load of 700 N, are shown in **Figure 4a and b**. In all cases the use of EP or AW additives reduced the steady-state friction and wear of the contact surfaces. However, the lowest values were obtained for the case of the DLC/steel combination. On the other hand, the DLC/DLC combination showed the highest wear, most

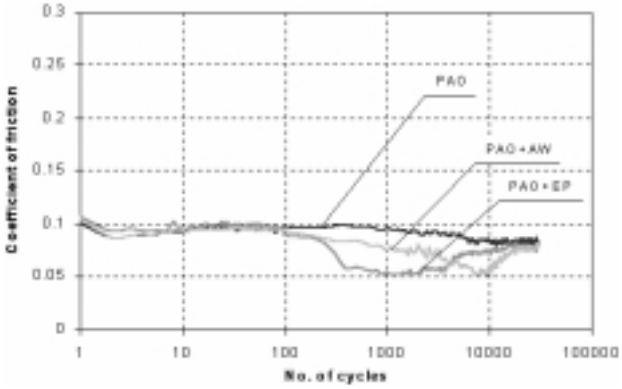

Figure 3: Friction curves for the DLC/steel combination, recorded at 700 N load
Slika 3: Koeficient trenja za kombinacijo DLC/jeklo; obremenitev 700 N

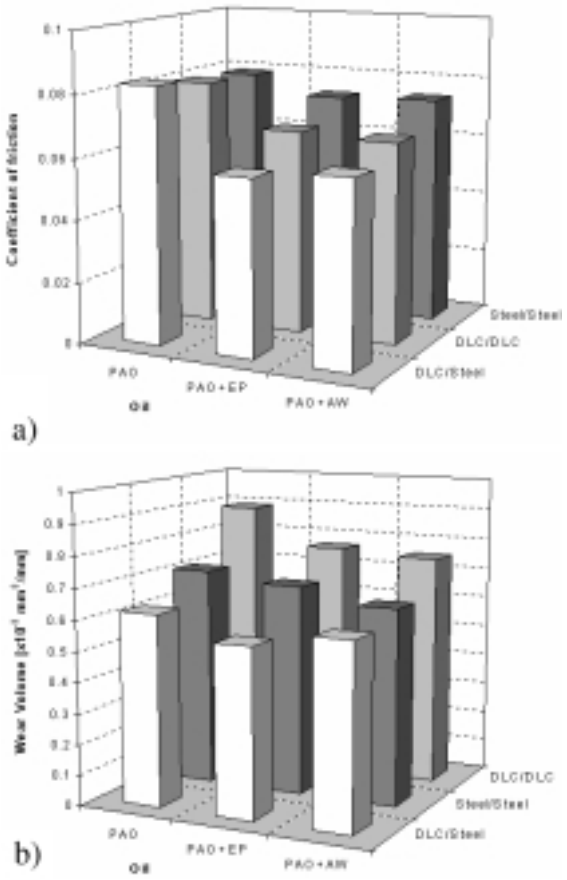

Figure 4: Minimum values of the coefficient of friction (a), and wear volume per unit length after 8,000 cycles (b); F_N = 700 N

Slika 4: Minimalna vrednost koeficienta trenja (a) in stopnja obrabe na enoto dolžine po 8.000 ciklih drsnega preizkusa (b); obremenitev 700 N

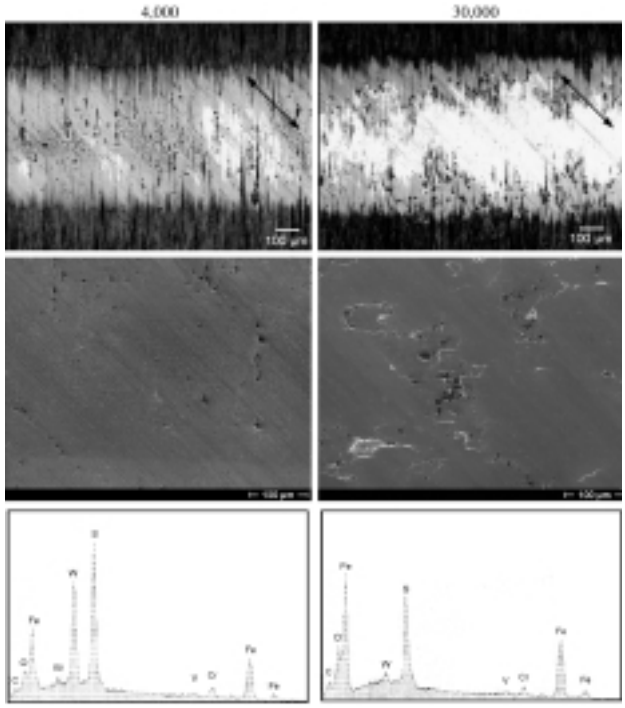

Figure 5: Optical micrographs of the sliding track on the DLC-coated specimen after 4,000 cycles (a) and 30,000 cycles (b), SEM micrographs of mating uncoated steel specimens (c and d) and corresponding EDS spectra (e and f); PAO+EP oil, F_N = 700 N

Slika 5: Kontaktna površina prekrita z DLC-prevleko po 4.000 (a) in 30.000 ciklih drsnega preizkusa (b), SEM-sliki jeklene protipovršine (c in d) ter pripadajoči EDS-spektri (e in f); PAO-olje + EP-aditiv, obremenitev 700 N

probably due to the contact of two hard, and initially rough, surfaces.

The deposition of a DLC coating gives lower initial friction and in the case of the DLC/steel combination a lower wear and a smoother running-in process, with the coefficient of friction below 0.1 from the very first stroke, as shown in **Figures 3 and 4**. The improved tribological properties can be explained by a faster smoothening of the steel surface and the transfer of coating material from the coated to the uncoated part. The use of the extreme-pressure (EP) or anti-wear (AW) additives had no effect on the frictional behaviour of the DLC-coated surfaces during running-in. Compared to the pure PAO oil, a similar wear mechanism, with only localised decohesion of the coating and no reaction of the additive with the coating material, was observed during the running-in period. Increasing the number of cycles led to a drop in the coefficient of friction, which coincides with the formation of a reaction film observed on areas where the coating has been worn off and on the uncoated steel counter-face, as shown in **Figure 5**. The reaction film was found to be composed of a combination of transferred coating material and reaction products from the additive, as indicated by the high concentrations of W and S for the EP-additive oil (**Figure 5e**), or W, S, Zn and P for AW-additive oil. After a certain number of cycles (10,000–20,000) the friction coefficient returned to the values observed for the steel/steel contact (~0.08). At this point the coating was completely removed from the surface and only a tribofilm consisting of reaction products from the additive could be detected in the contact surfaces, as shown in **Figure 5f**.

4 CONCLUSIONS

Deposition of a hard, low-friction DLC coating reduces the relatively high initial friction and leads to a smoother running-in process.

Standard EP and AW additives give up to 25% better tribological properties for DLC coated surfaces, as compared to pure PAO oil. The formation of a new tribofilm, composed of coating material and reaction products from the additives, was found to be responsible for the improved tribological behaviour observed.

The results of this investigation suggest that EP and AW additives react with the exposed steel surface and together with the transferred coating material form a new type of tribofilm. As soon as there is no more coating

material to support the formation of such a tribofilm, the friction coefficient reaches values typical for a steel/steel contact.

Acknowledgements

The Swedish Research Council and the Swedish Board for Strategic Research are acknowledged for their financial support. The supply of test oils and DLC coatings from Agroil and Balzers Sandvik Coating AB, respectively, is much appreciated.

5 REFERENCES

[1] O. Wanstrand, N. Axien, R. Fella, Surface and Coating Technologies, 94-95 (**1997**) 469

[2] C. Rincon, G. Zambrano, A. Carvajal, P. Prieto, H. Galindo, E. Martinez, A. Lousa, J. Esteve, Surface and Coating Technologies, 148 (**2001**) 277

[3] L. Rosado, V.K. Jain, H.K. Trivedi, Wear, 212 (**1997**) 1

[4] H. Ronkainen, S. Varjus, K. Holmberg, Wear, 222 (**1998**) 120

[5] B. Podgornik, Surface and Coating Technologies, 146-147 (**2001**) 318

[6] H. Ronkainen, S. Varjus, J. Koskinen, K. Holmberg, Wear, 249 (**2001**) 267

[7] W. Bartz, Additive fur Schmierstoffe, Expert verlag, Renningen, 1994

[8] S. Hogmark, S. Jacobson, O. Wanstrand: A new universal test for tribological evaluation, Proceedings of the 21st IRG-OECD Meeting, Amsterdam, 1999

[9] S. Hogmark, S. Jacobson, O. Wanstrand: The Uppsala Loadscanner – an Update, Proceedings of the 22st IRG-OECD Meeting, Cambridge, 2000

2 EXPERIMENTAL

$Sm_{13.7}Fe_{86.3}$ (SmFe) and $Sm_{13.8}Fe_{82.2}Ta_{4.0}$ (SmFeTa) cast alloys were produced by conventional induction melting by Less Common Metals. For the investigations in hydrogen the samples were crushed to a lump form and further reduced in size using a vibro-mill. For the investigations in nitrogen the material was first crushed and then further reduced in size by milling in hexane using an attritor mill for 30 minutes, in the inert atmosphere of a glove box, so as to produce a particle size of approximately 10 μm. All the thermo-magnetic experiments in hydrogen and nitrogen were performed using a Lakeshore 7303 VSM, modified with a high-temperature (up to 1000 °C) vacuum-gas system, offering the possibility to monitor the magnetic behavior of the samples during the hydriding or the nitriding process. The hydriding consisted of heating the samples in hydrogen to 750 °C at 5 °/min. Prior to heating in hydrogen the VSM's sample tube was twice evacuated to $8 \cdot 10^{-2}$ mbar. The cycles were repeated two times: Cycle 1 and Cycle 2. The nitriding of the milled-only samples, and the samples previously HDDR processed consisted of heating them in nitrogen to 450 °C at 5 °C/min.

3 RESULTS AND DISCUSSION

3.1 Experiments in hydrogen

Figure 1 shows the results from the SmFe alloy. For Cycle 1 (the black line) we see an initial drop in magnetization with temperature up to 125 °C, at which point we observe a rapid increase in magnetization - despite an increasing temperature. At 170 °C the magnetization ceases to increase any further, and from then on we observe a steady decline in the magnetization for about the next 200 °C, with the T_C of the hydrided Sm_2Fe_{17}-type phase found at 254 °C and that of the $SmFe_3$ phase at 386 °C. From this minimum in the magnetization further heating causes a steady increase between 398 °C and 505 °C before a more rapid increase takes place up to 598 °C. The magnetization of the sample then decreases at an increasing rate until the end of the experiment at 750 °C. Cycle 2 (the dark-gray line) contains the same basic reactions and T_Cs as Cycle 1 but with some significant differences. The initial hydrogenation reaction has clearly divided into two separate reactions. As with Cycle 1 the magnetization then decreases and the hydrided Sm_2Fe_{17}-type phase has its T_C again at 254 °C. At ~380 °C there is almost no indication of any T_C, however, there is still clear evidence for a smaller disproportionation reaction associated with the $SmFe_3$ phase. Compared to Cycle 1, the main disproportionation reaction of the Sm_2Fe_{17}-type phase is now much faster.

Figure 2 shows the results from the SmFeTa alloy. Although similar to the SmFe alloy in their basic forms, it exhibits some important differences. The initial hydrogenation reaction remains single-stage for both cycles, with the second cycle seeing the start of the reaction at a higher temperature: Cycle 1, 141 °C; and Cycle 2, 160 °C. After a peak in the magnetization the curves indicate a T_C for the material as follows: Cycle 1, 250 °C; and Cycle 2, 257 °C. In the high-temperature part of the graph it is clear that the Cycle-1 curve is very different from the subsequent one. Not only does it exhibit a T_C at 388 °C and a subsequent disproportionation beginning at 402 °C, but the main disproportionation of the Sm_2Fe_{17}-type phase is much slower with the peak in the magnetization not occurring until 702 °C, in comparison with 660 °C for Cycle 2 and less than 600 °C for all of the SmFe-alloy cycles.

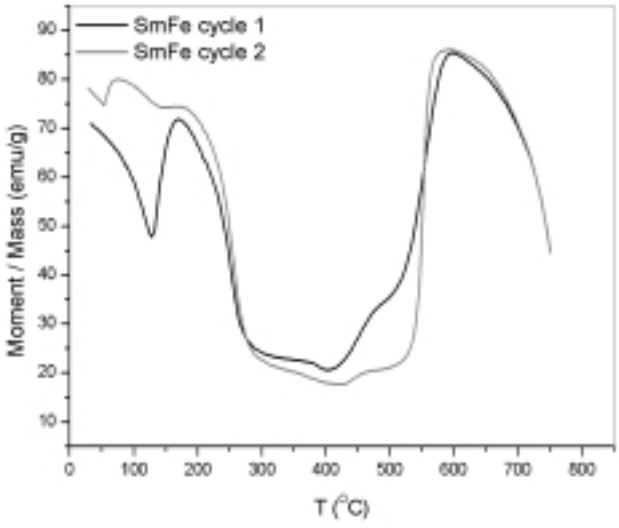

Figure 1: The curve representing the moment/mass in Cycle 1 and Cycle 2 vs. temperature for the SmFe sample in hydrogen

Slika 1: Krivulja moment/masa za vzorec SmFe v vodiku v odvisnosti od temperature

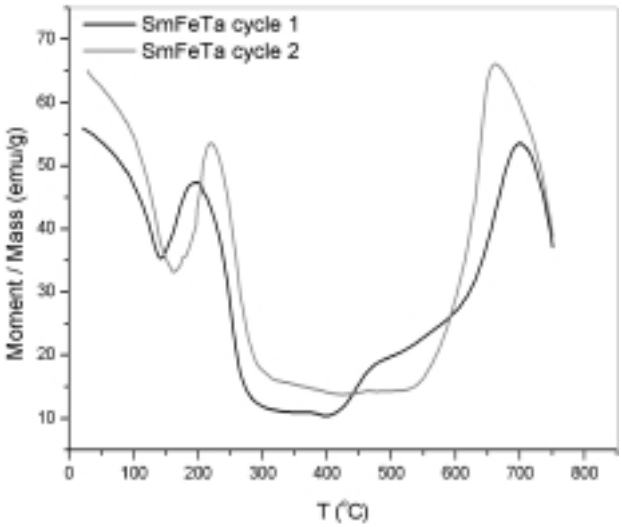

Figure 2: The curve representing the moment/mass in Cycle 1 and Cycle 2 vs. temperature for the SmFeTa sample in hydrogen

Slika 2: Krivulja moment/masa za vzorec SmFeTa v vodiku v odvisnosti od temperature

The hydrogenation of the Sm_2Fe_{17}-type phase of the $Sm_{13.7}Fe_{86.3}$ (SmFe) material depends on the number of the HDDR cycles to which the material has been subjected. The initial absorption reaction is a surface-dependent process, which explains the shift from an initial single absorption at 125 °C to a two-stage absorption at 54 °C and 149 °C. The three-component $Sm_{13.8}Fe_{82.2}Ta_{4.0}$ (SmFeTa) material behaves in a more consistent way with the second HDDR cycle delaying the onset of the hydrogenation. Additional differences were found in the T_Cs of the hydrided Sm_2Fe_{17}-type phases for SmFe and SmFeTa. For both cycles we obtained a value of 254 °C - in almost exact agreement with Xiang-Zhong et al [12] - for the SmFe material, but for the SmFeTa material the T_C increased after the first cycle: from 250 °C during Cycle 1 to 257 °C. Such a result suggests that the material may not have been fully hydrided during the first cycle and/or a significant change had taken place in the material after the first HDDR cycle. Between 300 °C and 400 °C the SmFe and SmFeTa materials behave in a very similar manner. Both materials show evidence for the presence of the $SmFe_3$ phase with a T_C at 386 °C (SmFe) and 388 °C (SmFeTa). The fact that these T_Cs are 9 °C and 11 °C above the reported value for $SmFe_3$ [5] suggests that the material still contains some hydrogen at the onset of the disproportionation at 398 °C (SmFe) and 402 °C (SmFeTa). It is also clear that the HDDR cycling reduces the amount of $SmFe_3$ phase present. For both materials there is practically no evidence for the existence of this phase after the first HDDR cycle.

The disproportionation of the $SmFe_3$ phase overlaps to some extent with the onset of the disproportionation of the Sm_2Fe_{17}-type phase. Nevertheless, for the SmFe material we can easily see the effects of repeated HDDR cycling. During the first cycle the reaction begins at about 500 °C and reaches a maximum rate of 0.93 emu g^{-1} $°C^{-1}$ at 554 °C before tailing off with a maximum in the magnetization at 598 °C. From this point on the magnetization is solely a consequence of the presence of iron and if the experiment were continued beyond 750 °C we would see the T_C of the iron at 768 °C. The second cycle produced almost identical disproportionation reactions with a maximum rate of 3.44 emu g^{-1} $°C^{-1}$, at 550 °C. This small difference in the point of maximum-magnetization increase of only 4 °C for the SmFe material is in stark contrast to the difference between the first and second cycles for the SmFeTa material. During Cycle 1 for the SmFeTa we see a much slower start to the reaction with a peak in the disproportion rate of 0.39 emu g^{-1} $°C^{-1}$ at 663 °C. Cycle 2 has a peak reaction rate of 0.79 emu g^{-1} $°C^{-1}$ at 617 °C - some 46 °C lower. The difference in the temperature of maximum disproportionation rate for the SmFe and SmFeTa alloys on the first cycle is just over 100 °C, very similar to the result we obtained previously using a gas-flow-analysis technique [13].

The slower disproportionation reaction of the SmFeTa material, particularly during Cycle 1, suggests that the tantalum must be stabilizing the Sm_2Fe_{17}-type phase. The difference in the disproportionation reaction between Cycle 1 and Cycle 2 for the same material suggests that the tantalum plays a less important role after the completion of the first cycle. This is also born out by the initial hydriding behavior of the SmFeTa. During Cycle 1 we obtained a T_C of 250 °C while heating the sample in hydrogen, the next cycle gave us a value of 257 °C - whereas the values obtained for the SmFe material stayed the same for both cycles - suggesting that some alteration in the chemistry had occurred. These observations are in very good agreement with our earlier EDX studies on these materials [13], which indicated that the initial concentration of tantalum dissolved in the Sm_2Fe_{17}-type phase was 2.0±0.1 atomic %. After a single HDDR cycle this same phase contained only 1.2±0.1 atomic % of dissolved tantalum, however, it now had Ta_3Fe_7 nano-precipitates distributed within the phase.

3.2 Experiments in nitrogen

The in-situ magnetic changes during the nitrogenation for SmFe are presented in **Figure 3**. The difference in magnetic behavior between the milled-only and the milled+HDDR-ed material is obvious. The milled+HDDR-ed material reacts with nitrogen in a very straightforward way. The magnetization of the material decreases with increasing temperature and the Curie temperature of the Sm_2Fe_{17} phase is observed at 141 °C. The magnetization continues to decrease up to the temperature of 240 °C, when the nitrogen starts to diffuse into the 2:17 lattice. Because of lattice expansion the magnetization starts to increase and reaches a maximum rate of 0.47 emu g^{-1} $°C^{-1}$ at 360 °C. The end temperature of the experiment was based on our previous investigations, in which we discovered that 450 °C is the optimum nitriding temperature. It is clear that the reaction is close to completion at 450 °C. The nitrogen behavior of the milled-only sample differs from the milled+HDDR-ed sample in several aspects. The slight initial magnetization increase at 102 °C is due to the thermal relaxation of the magnetic moments in the material. As the temperature increases the material demagnetizes and the Curie point of the Sm_2Fe_{17} phase is observed at 141 °C. The magnetization increase at around 250 °C, attributed to the absorption of nitrogen into the 2:17 phase, overlaps with an additional process, which gives rise to the magnetization changes in the region between 150 and 300 °C. As a consequence the initial nitrogen absorption temperature for this material cannot be determined. After the magnetization reaches a minimum at 290 °C a steady increase is observed, but with a slower rate (0.20 emu g^{-1} $°C^{-1}$) than the milled+ HDDR-ed material.

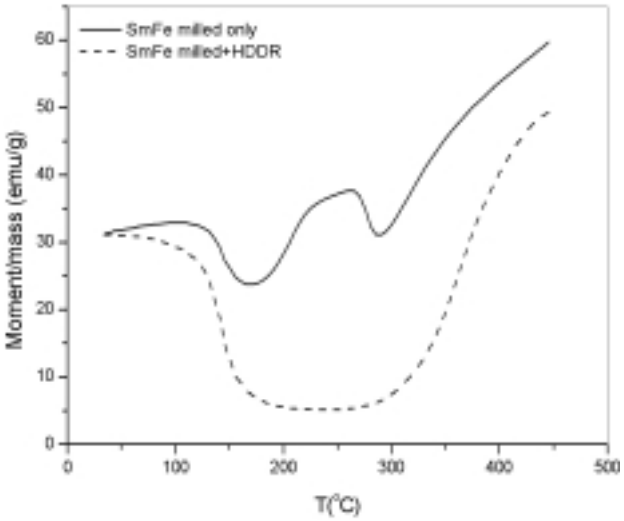

Figure 3: The curve representing the moment/mass vs. temperature for the milled-only and milled+HDDR-ed SmFe samples in nitrogen

Slika 3: Krivulja moment/masa za vzorec SmFe (samo mlet in mlet + obdelan po postopku HDDR) v dušiku v odvisnosti od temperature

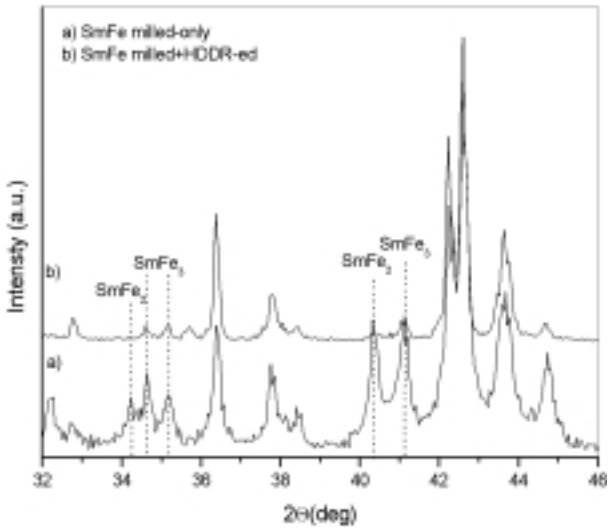

Figure 5: XRD patterns for the SmFe sample: a) milled only, b) milled+HDDR-ed

Slika 5: Rentgenska difraktograma za vzorec SmFe: a) samo mlet, b) mlet + obdelan po postopku HDDR

The SmFeTa alloy presented in **Figure 4** reacts with nitrogen in a very similar way to SmFe alloy. The magnetization of the HDDR-ed material decreases with increasing temperature, and the Curie temperature is observed at 150 °C. The nitrogen absorption starts at 225 °C and reaches a maximum rate of 0.29 emu g^{-1} $°C^{-1}$ at 350 °C. At 450 °C the magnetization is still increasing. The behavior of the milled-only material while heating in nitrogen again differs from the milled+HDDR-ed material, which behaves in a similar way to the binary alloy. The magnetization in the temperature region between 150 °C and 350 °C shows two peaks, one at 225 °C and the next one at 280 °C. After the magnetization reaches minimum at 305 °C it starts to increase again with rate 0,39 emu g^{-1} $°C^{-1}$, until 400 °C, where it stabilizes.

The different behavior of the milled-only and milled+HDDR-ed material can be explained by taking several factors into consideration. The first difference between them is in the microstructure. The milled-only material is not homogeneous, and it has a lot of irregularities that result from previous material preparation methods such as casting and milling. The grain size of the milled-only sample is large in comparison with the HDDR-processed material, which is a relatively homogeneous sample with a uniform sub-micron grain

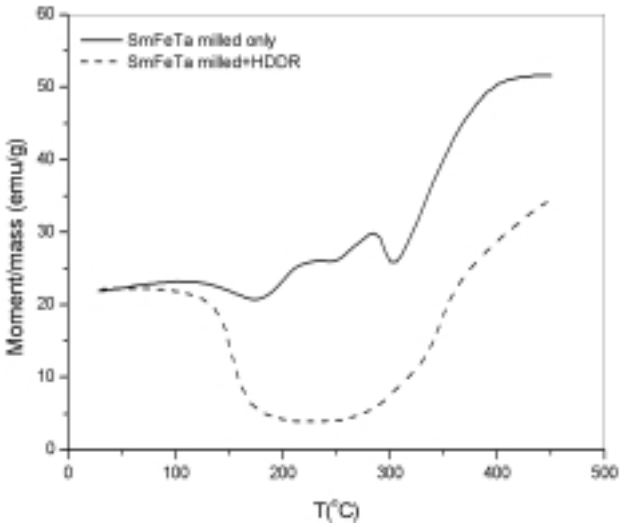

Figure 4: The curve representing the moment/mass vs. temperature for milled-only and milled+HDDR-ed SmFeTa samples in nitrogen

Slika 4: Krivulja moment/masa za vzorec SmFeTa (samo mlet in mlet + obdelan po postopku HDDR) v dušiku v odvisnosti od temperature

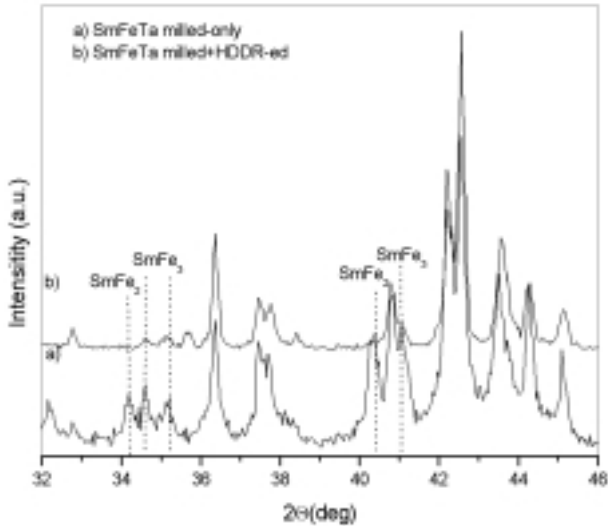

Figure 6: XRD patterns for the SmFeTa sample: a) milled only, b) milled+HDDR-ed

Figure 6: Rentgenska difraktograma za vzorec SmFeTa: a) samo mlet, b) mlet + obdelan po postopku HDDR

size. Therefore, one explanation is in the different characteristics of the samples before and after the HDDR processing. But this is not the only difference between the milled-only and milled+HDDR-ed samples. They also differ in terms of their phase composition. From our previous experiment in hydrogen it is clear that the HDDR process reduces the amount of $SmFe_3$ phase in both the SmFe and SmFeTa samples. In order to thoroughly investigate the phase composition the milled-only and milled+HDDR-ed samples were examined using XRD. The patterns are presented in **Figures 5 and 6**. The a) patterns present the phase composition of the milled-only samples. The peaks of the Sm_2Fe_{17} phase as well as the peaks from $SmFe_2$ and $SmFe_3$ phases are observed for both the SmFe and SmFeTa samples. The pattern of the milled+HDDR-ed sample differs from the milled-only. The peaks of the Sm-rich phases have shrunk significantly which leads us to believe that the different behavior during nitrogenation is due to the disproportionation of the Sm-rich phases ($SmFe_2$ and $SmFe_3$), which are present in the as-cast material. These phases decompose during heating in nitrogen to SmN and αFe, which gives rise in the increase in the magnetization. It was previously reported that these phases decompose in nitrogen at temperatures above 450 °C [14]. It was also reported that the reaction of the Sm-rich phases is particle-size dependent [5,6]. Therefore, we believe that because of the very fine powder the phases react and decompose in nitrogen at even lower temperatures than have been reported so far. The nitrogen absorption process for the Sm_2Fe_{17} phase in the milled-only samples overlaps with the disproportionation of the Sm-rich phases, therefore, the process is not so clear as with the samples which were previously HDDR processed.

4 CONCLUSIONS

By using a VSM, a device that can be accurately calibrated in terms of both the temperature and the magnetic moment of the sample, we have a method that can give us precise information about chemical reactions that result in changes to the magnetic state of iron as well as the T_Cs of phases as they absorb and desorb hydrogen or nitrogen.

The behavior in hydrogen depends on the number of cycles to which the material is subjected. The elimination of Ta from the 2:17 phase shifts the disproportionation reaction to lower temperatures.

The behavior during nitriding depends on the sample processing as well as the sample composition. The reason for the different nitrogen behavior between the milled-only and milled+HDDR-ed material is the removal of the Sm-rich phases during the HDDR process, as well as grain refinement and homogenization.

Acknowledgements

The Ministry of Science, Technology and Sport of the Republic of Slovenia is gratefully acknowledged for its financial support of this research.

5 REFERENCES

[1] J. M. D. Coey, H. Sun, J. Magn. Magn. Mater., 87 (**1991**) L251
[2] A. E. Platts, I. R. Harris, J. M. D. Coey, J. Alloys. Comp., 185 (**1992**) 251
[3] B. Saje, A. E. Platts, S. Kobe Beseničar, I. R. Harris, D. Kolar, IEEE Trans. Magn., 30 (**1994**) 690
[4] B. Gebel, M. Kubis, K.-H. Muller, J. Magn. Magn. Mat., 174 (**1997**) L1
[5] C. Christodoulu, T. Takeshita, J. Alloys. Comp., 194 (**1993**) 31
[6] C. Christodoulu, T. Takeshita, J. Alloys. Comp., 191 (**1993**) 279
[7] M. Zinkkevich, N. Mattern, A. Handstein, O. Gutfleisch, J. Alloys. Comp., 339 (**2002**) 118
[8] T. Hidaka, Y. Yamamoto, H. Nakamura, A. Fukuno, J. Appl. Phys., 83 (**1998**) 11, 6917
[9] F. Kawashima, S. Sakurada, T. Sawa, T. Arai, A. Tsutai, M. Sahashi, IEEE Trans. Mag., 35 (**1999**) 5, 3289
[10] Z. Liu, T. Ohsuna, K. Hiraga, M. Tobise, J. Alloys. Comp., 288 (**1999**) 277
[11] K. Žužek, P. J. McGuiness, S. Kobe, J. Alloys. Comp., 289 (**1999**) 265
[12] W. Xiang-Zhong, K. Donnelly, J. M. D. Coey, B. Chevalier, J. Etourneau, T Berlureau, J. Mat. Sci., 23 (**1988**) 329
[13] K. Žužek, P. J. McGuiness, G. Dražič, S. Kobe, Zeitschrift für Metallkunde, 92 (**2001**) 167
[14] C. Ishizaka, T. Yoneyama, A. Fukuono, IEEE Trans. Mag., 29 (**1993**) 6, 2833

UDK 539.42
Izvirni znanstveni članek

ISSN 1580-2949
MTAEC9, 37(1-2)39(2003)

NUMERIČNA IN EKSPERIMENTALNA ANALIZA UTRUJANJA V LOMNOMEHANSKEM PRESKUŠANCU NESTANDARDNE OBLIKE

NUMERICAL AND EXPERIMENTAL ANALYSES OF FATIGUE IN A NON-STANDARD FRACTURE-MECHANICS SPECIMEN

Igor Kovše

Inštitut za metalne konstrukcije, Mencingerjeva 7, 1001 Ljubljana, Slovenija
igor.kovse@imk.si

Prejem rokopisa - received: 2002-12-09; sprejem za objavo - accepted for publication: 2003-03-11

V prispevku je prikazana numerična simulacija rasti utrujenostne razpoke pri mešanem lomnem načinu. Postopek je avtomatiziran do te mere, da je kot vhodni podatek potrebno podati le obris območja tj. preskušanca, začetno mesto razpoke in materialne parametre, kot končni rezultat pa med drugim dobimo pot razpoke in odnose $K_I(a)$, $K_{II}(a)$, $N(a)$, tj. faktorja intenzitete napetosti in število ciklov v odvisnosti od dolžine razpoke. Za numerične izračune je uporabljena metoda končnih elementov. Rast utrujenostne razpoke je simulirana z vrsto prirastkov razpoke končne dolžine. Mreža končnih elementov je po vsakem prirastku razpoke generirana avtomatično. Numerični rezultati so primerjani s preskusom na preskušancu nestandarne oblike. Med preskusom smo na osnovi izmerjene podajnosti sproti določali tudi dolžino razpoke.

Ključne besede: utrujanje, mehanika loma, končni elementi, pot razpoke

This paper presents a numerical simulation of crack propagation in mixed mode fatigue. The procedure is automatic in so far as only the specimen's geometry, the starting point of the crack and the material parameters are needed as input, and the output is the crack path, and the functions $K_I(a)$, $K_{II}(a)$, $N(a)$, i.e. stress-intensity factors and the number of cycles depending on the crack length a. The finite-element method is used in the calculation. Crack growth is simulated in a series of crack increments of finite size. The finite-element mesh is automatically generated after each crack increment. The numerical results are compared to the results of the experiment on a specimen with non-standard geometry. During the experiment the crack length was measured automatically from the compliance of the specimen.

Key words: fatigue, fracture mechanics, finite elements, crack path

1 UVOD

Motivacija za analizo vpliva razpok na vedenje konstrukcij, predvsem kovinskih, temelji na naslednjih dejstvih:

- Velik delež porušitev in poškodb konstrukcij v obratovanju ima za vzrok razpoko ali razpoki podobno napako v materialu.
- Manjša nosilnost elementov, ki so obremenjeni s ponavljajočo se obremenitvijo, tj. z utrujanjem, je posledica nastanka in rasti razpok.
- Materiali z višjo trdnostjo in elementi z večjimi debelinami - kar je usmeritev današnjega razvoja - so večkrat manj žilavi oziroma bolj občutljivi za razpoke.
- Razpoka lahko privede do hipnih porušitev brez na zunaj vidnih deformacij ali poškodb, ki bi nakazovale nevarnost porušitve.
- Poznanje zakona rasti razpok omogoča oceno trajnostne dobe konstrukcij.

Vpliv razpok na vedenje konstrukcije lahko zajamemo posredno z njihovim vplivom na materialne parametre. Ta način, s tako imenovanimi "razmazanimi" razpokami, se pogosto uporablja v mehaniki poškodbe. Drugi način, ki ga uporablja mehanika loma, je upoštevanje dejanske geometrije razpoke kot dve različni a geometrijsko ujemajoči se ploskvi. Tak način je uporabljen tudi v nadaljevanju.

Pri uspešni analizi razpok v konstrukciji moramo kvantitativno odgovoriti vsaj na dve naslednji vprašanji:

1. *Kakšna je odvisnost med nosilnostjo konstrukcije ali njenega elementa in velikostjo razpoke?*

To odvisnost ponazorimo z neenačbo:

$$K_I(a,P) \le K_{Ic} \tag{1.1}$$

K_{Ic} je lomna žilavost in je lastnost materiala, faktor intenzitete napetosti K_I pa je računska vrednost odvisna od geometrije elementa konstrukcije z razpoko, obtežbe P in dolžine razpoke a. Enakost v zgornji neenačbi pomeni, da je doseženo kritično stanje ob porušitvi.

2. *Kako dolgo traja, da razpoka določene začetne velikosti naraste do neke končne (navadno kritične) velikosti?*

Odgovor dobimo z integracijo naslednje enačbe o hitrosti rasti razpoke $\dot{a}$:

$$\dot{a} = \frac{da}{dt} = F(K_I(a,P)) \tag{1.2}$$

Funkcijo F določimo iz dinamičnega preskusa, pri katerem vzorec obremenjujemo z obtežbo P, ki se periodično spreminja s časom t.

Analiza je torej kombinacija numeričnih in eksperimentalnih metod, kjer odvisnost $K_I(a,P)$ določamo z numeričnim izračunom, materialno lastnost K_{Ic} in funkcijo F pa s preskusi. V nadaljevanju je ta postopek prikazan za nestandardni lomnomehanski vzorec, ki smo ga imenovali CTN, kjer za $K_I(a)$ ne obstajajo analitične ali numerične rešitve. Vzorec CTN je nekoliko spremenjeni standardni lomnomehanski CT vzorec, vendar ga lahko imamo za detajl, ki je kritičen za vedenje hipotetične konstrukcije. Z nestandarno geometrijo smo nameravali pokazati, kako se principi lomne mehanike ob primerno razvitih numeričnih in eksperimentalnih metodah lahko uporabijo pri analizi napredovanja razpoke - tj. utrujanja - v poljubnem konstrukcijskem detajlu.

2 RAČUN ODVISNOSTI $K_I(a,P)$

Odnos $K_I(a,P)$ potrebujemo za določitev kritičnega stanja po enačbi (1.1) in za prikaz hitrosti rasti razpoke po enačbi (1.2). Faktor intenzitete napetosti K_I je linearno odvisen od sile P, zato se problem določanja $K_I(a,P)$ prevede le na določitev odvisnosti $K_1(a)$, kjer K_1 pomeni K_I pri enotni sili P. Za nekatere (enostavnejše, standardizirane) primere je ta odnos znan v analitični obliki, v splošnem pa ga je treba določiti numerično.

Določevanje odnosa $K_I(a)$ je le eden izmed rezultatov numerične simulacije rasti razpoke. Simulacija, ki je prikazana v tem prispevku, temelji na metodi končnih elementov (MKE).

Vhodni podatki za simulacijo so obris področja v ravnini z določeno točko, v kateri se razpoka začne, in karakteristike obravnavanega materiala. V našem primeru je to obris vzorca CTN (modificirani CT vzorec) s **slike 2.1** z dimenzijami: širina W = 50 mm, debelina B = 25 mm, začetna dolžina razpoke a_0 = 24,5 mm, velikost izreza w = 14 mm. Podobno obliko preskušanca je analiziral že Lining [2]. Upoštevali smo linearno elastični

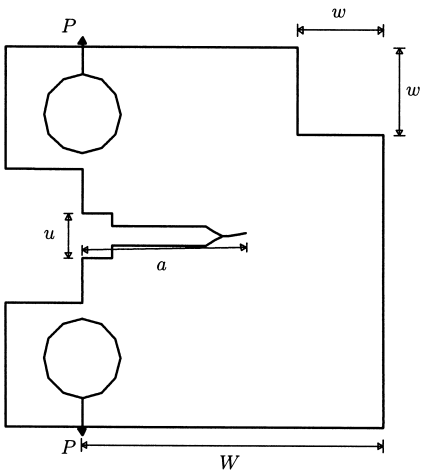

Slika 2.1: Obris vzorca CTN kot vhodni podatek za numerično analizo

Figure 2.1: The contour of the CTN specimen as the input to the numerical analysis

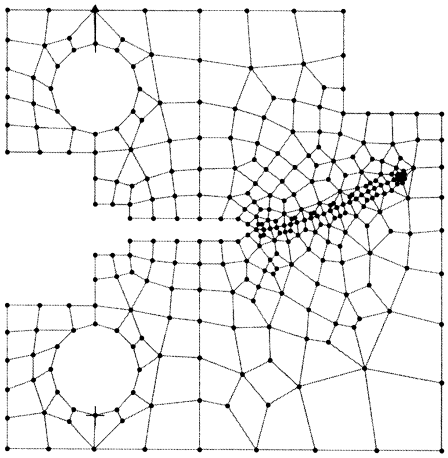

Slika 2.2: Mreža končnih elementov, generirana avtomatično pri dolžini razpoke a = 39 mm

Figure 2.2: The finite-element mesh generated automatically at the crack length a = 39 mm

material s parametroma za jeklo: modul elastičnosti E = $2{,}1 \cdot 10^5$ MPa in Poissonov količnik ν = 0,3. Vzorec je bil narejen iz konstrukcijskega jekla s povišano napetostjo tečenja (σ_y = 430 MPa) z oznako S355J2H po standardu EN 10210-1.

Rast razpoke simuliramo z vrsto diskretnih prirastkov razpoke Δa, pri čemer uporabimo avtomatično generacijo mreže končnih elementov pri vsakem prirastku razpoke znova (**slika 2.2**). Generator mreže temelji na algoritmu [3] in je podrobno opisan v [4]. Po vsaki generirani mreži izračunamo pomike, deformacije in napetosti po standarnem MKE-postopku, nato pa računamo parametre linearno elastične mehanike loma - K_I, K_{II}, J, G in smer rasti razpoke ϕ.

Parametre mehanike loma računamo z metodo virtualne rasti razpoke (VCE) [5]. Gre za metodo, po kateri vrh razpoke podaljšamo za majhno vrednost (reda velikosti 1/1000 dolžine končnega elementa ob vrhu razpoke), nato pa iz razlik potencialnih energij pred podaljšanjem razpoke in po njem izračunamo hitrost sproščanja deformacijske energije G. Z razčlenitvijo pomikov na simetrični in nesimetrični del [6] lahko po istem postopku izračunamo G_I in G_{II}, ki ustrezata lomnima načinoma I in II, iz teh vrednosti pa K_I in K_{II}. Kot ϕ nam podaja smer naslednjega prirastka razpoke. Določimo ga kot smer, v kateri hitrost sproščanja deformacijske energije G doseže maksimum [7].

Z vrsto zaporednih prirastkov razpoke dobimo tako pot razpoke, odvisnost $K_I(a)$ od dolžine razpoke a in podobno tudi odvisnosti $K_{II}(a)$, $J(a)$, $G(a)$, $\phi(a)$.

Za CTN vzorec smo po zgoraj opisani metodi dobili potek $K_I = K_I(\alpha)$ kot je prikazan na **sliki 2.3**. Tukaj smo z $\alpha = a/W$ označili normirano dolžino razpoke. Če poznamo lomno žilavost materiala K_{Ic}, lahko iz tega diagrama določimo kritično dolžino razpoke $a_c = \alpha_c W$ kot je prikazano na **sliki 2.3**. Razpoka pri tem vzorcu ne poteka premočrtno (glej **sliko 4.1**). Dolžino razpoke a zato tukaj

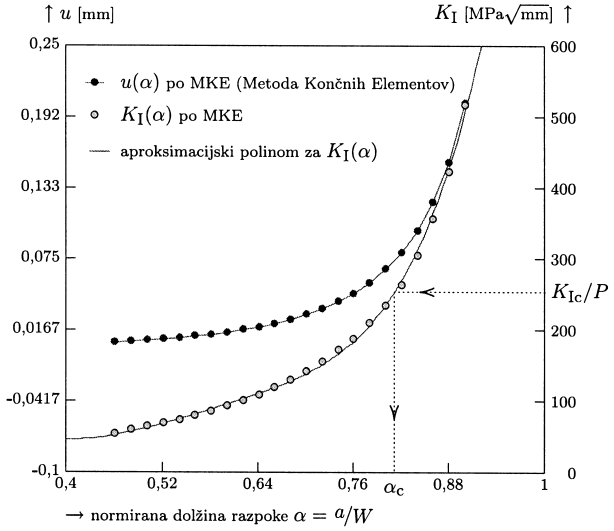

Slika 2.3: Numerična analiza po MKE. Odvisnosti pomika $u = u(\alpha)$ in $K_I = K_I(\alpha)$ za vzorec CTN in za enotno silo P = 1 kN
Figure 2.3: FEM analysis. The dependencies $u = u(\alpha)$ and $K_I = K_I(\alpha)$ for the CTN model and the unit force P = 1 kN.

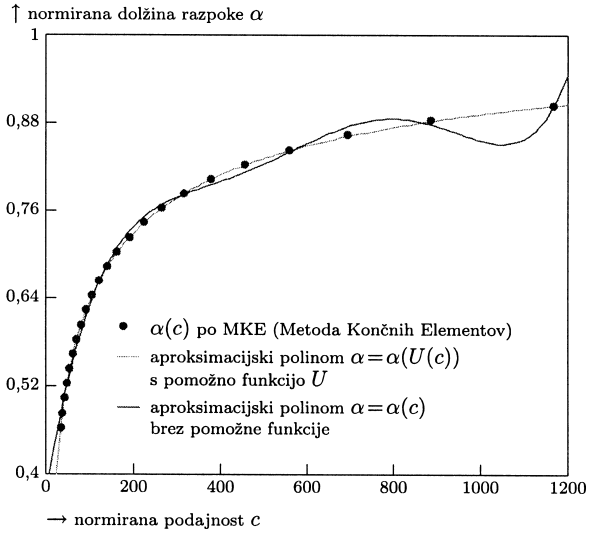

Slika 3.1: Odvisnost $\alpha = \alpha(c)$ za vzorec CTN in aproksimacijska polinoma z in brez pomožne funkcije U
Figure 3.1: The relation $\alpha = \alpha(c)$ for the CTN specimen and the approximation polynomials, with and without the auxiliary function U

jemljemo kot ločno dolžino - čeprav bi lahko za nadaljnje izvajanje vzeli tudi kako drugačno definicijo za a.

3 DOLOČANJE DOLŽINE RAZPOKE IZ PODAJNOSTI

Podajnost $C = u/P$ je definirana kot razmerje med pomikom u v določeni točki telesa in silo P, ki deluje na to telo. Pri podaljšanju razpoke a se (pri enaki sili P) spremeni pomik u, zaradi tega pa tudi podajnost C. Odnos $C = C(a)$ je v splošnem nelinearen. Navadno uporabimo normirano podajnost c, ki jo definiramo s $c = C \cdot B \cdot E$. Odnos med dolžino razpoke a in podajnostjo vzorca c oziroma inverzno funkcijo $a = a(c)$ lahko uporabimo pri meritvi dolžine razpoke med utrujenostnim preskusom. Z zgoraj opisano numerično metodo določimo funkcijo $a = a(c)$ na naslednji način.

Odnos $u = u(\alpha)$ (**slika 2.3**) oz. $c = c(\alpha) = u(\alpha)/P$ dobimo na enak način kot odnos $K_I(a)$: z zaporednimi numerični rešitvami po MKE ob podaljševanju dolžine razpoke a.

Inverzno funkcijo $\alpha = \alpha(c)$ aproksimiramo s polinomom po metodi najmanjših kvadratov [8]. Funkcija $\alpha(c)$ ima obliko, ki se po navadi ne da zadovoljivo aproksimirati s polinomom, zato je treba uporabiti pomožno funkcijo U. Priporočljivo je to funkcijo izbrati v obliki:

$$U(c) = \frac{1}{\sqrt{c}+1}$$

in namesto funkcije $\alpha = \alpha(c)$ računati s funkcijo $\alpha = \alpha(U(c))$. Na osnovi numerično dobljenih vrednosti za $c = c(\alpha)$ smo tako določili aproksimacijski polinom za vzorec CTN

$$\alpha(U(c)) = k_0 + k_1 U + k_2 U^2 + k_3 U^3 + k_4 U^4 \qquad (3.1)$$

s koeficienti

k_0 = 1,0660, k_1 = -6,2426, k_2 = 17,688, k_3 = -2,9554, k_4 = -150,78

Dobro ujemanje aproksimacijskega polinoma z numeričnimi vrednostmi je razvidno s **slike 3.1**. S te slike je tudi razvidno, da dobimo popolnoma neprimerno aproksimacijo za odnos $\alpha = \alpha(c)$, če ne uporabimo funkcije U.

4 UTRUJENOSTNI PRESKUS VZORCA IN PRIMERJAVA Z RAČUNOM

Za določitev zakona F iz enačbe (1.2) naredimo preskus, pri katerem vzorec obremenjujemo s silo, ki se periodično spreminja s frekvenco f in amplitudo $\Delta P = P_{max} - P_{min}$. Pri tem štejemo število ciklov obremenitve N in merimo dolžino razpoke a. Dolžino razpoke lahko merimo kar iz podajnosti C. Namreč s sprotno meritvijo sile P in pomika u določimo podajnost $C = u/P$, iz odnosa $\alpha = \alpha(c)$, ki smo ga določili v prejšnjem poglavju, pa izračunamo dolžino razpoke a. Z izmerjenimi a in N in računsko določenim $K_I(a,P)$ lahko določimo funkcijo F iz enačbe (1.2).

V nadaljevanju prikazujemo rezultate preskusa in računa za nestandardni vzorec CTN. Pri preskusu smo vzorec CTN obremenjevali s ciklično obremenitvijo s frekvenco f = 4 Hz, s konstantno amplitudo sile ΔP = 10 kN in z razmerjem sil $R = P_{min}/P_{max}$ = 0,2. Na **sliki 4.1** je primerjava numerično določene poti razpoke z obliko razpoke pri preskusu vzorca.

Med preskusom smo določali dolžino razpoke a iz izmerjene podajnosti c po enačbi (3.1). Za kontrolo smo dolžino razpoke merili tudi z optičnim mikroskopom. Primerjava obeh metod je na **sliki 4.2**.

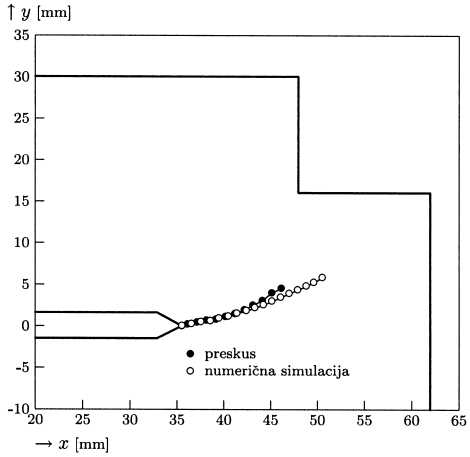

Slika 4.1: Primerjava numerično simulirane poti razpoke in dejanske oblike razpoke po utrujenostnem preskusu
Figure 4.1: Comparison of the numerically simulated crack path with the experimental crack path

Za določitev funkcije F iz enačbe (1.2) potrebujemo odvod *da/dt* oziroma odvod *da/dN*, saj velja $da/dt = da/dN \cdot dN/dt = da/dN \cdot f$. Direktno računanje odvoda *da/dN* iz izmerjenih parov vrednosti (a,N) (tj. z diferenčnim kvocientom) ni primerno, ker prihaja do velikega raztrosa rezultatov ([9], glej tudi **sliko 4.3**). Zaradi tega smo izmerjeno krivuljo $a = a(N)$ aproksimirali z eksponentno funkcijo $y(N) = A + e^{(C \cdot N + D)^B}$ (prikazana je na **sliki 4.2**) in z odvajanjem te funkcije določili hitrost razpoke $da/dN = dy/dN = y'$. Neznane koeficiente A,B,C,D v funkciji $y(N)$ smo določili po posebnem postopku [9]:
$A = 24{,}5$, $B = 9{,}9902$, $C = 11{,}02\ 10^{-6}$, $D = 0{,}3417$

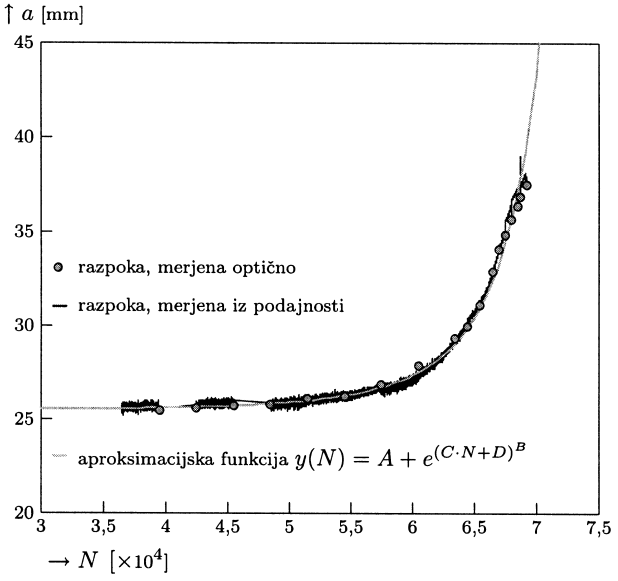

Slika 4.2: Dolžina razpoke v odvisnosti od števila ciklov. Primerjava dveh metod merjenja razpoke: iz podajnosti in optično
Figure 4.2: Crack length as a function of the number of cycles. Comparison of two measurement methods: optical and compliance methods.

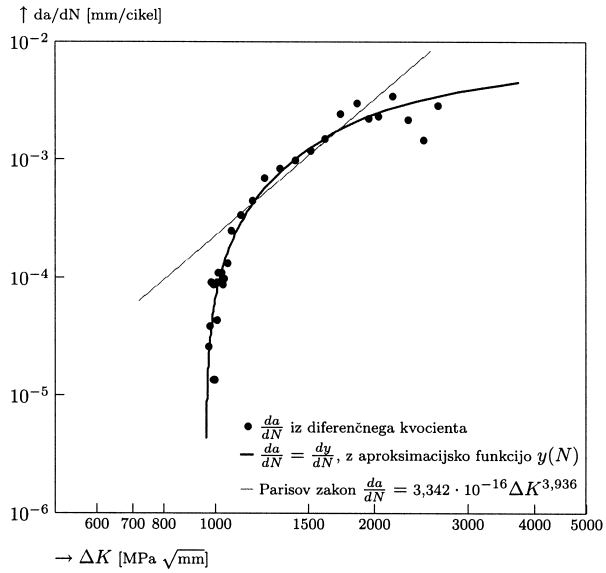

Slika 4.3: Zakon hitrosti rasti razpoke. Vrisane so vrednosti *da/dN*, dobljene z numeričim odvajanjem izmerjenih vrednosti (z diferenčnim kvocientom), z odvajanjem aproksimacijske funkcije in Parisov zakon.
Figure 4.3: The crack-growth rate law from the experiment on the CTN specimen. The values of *da/dN* are obtained with numerical differentiation of the measured values and with the differentiation of the approximating function $y(N)$. Also shown is the Paris line.

Z znanimi funkcijami $a = y(N)$, $da/dN = y'$ in $\Delta K_I(a) = \Delta P K_1(y(N))$ poznamo tudi odnos F. Za opravljen preskus na CTN-vzorcu je ta odnos narisan na **sliki 4.3**. Lahko ga uporabimo pri integraciji enačbe (1.2) namesto standardne Parisove krivulje, ki v logaritemskem merilu pomeni linearizacijo dela tega odnosa.

5 SKLEP

Prikazana je numerična in eksperimentalna analiza utrujenostne razpoke pri nestandardni geometriji preskušanca. Numerična simulacija je bistveno poenostavljena z uvedbo avtomatičnega generiranja mreže končnih elementov po vsakem prirastku razpoke. S simulacijo dobimo odvisost poljubnega lomnomehanskega parametra od dolžine razpoke. Razen tega je s simulacijo mogoče zadovoljivo napovedovati razvoj tudi nesimetričnih, tj. zakrivljenih razpok. Rezultati simulacije so uporabljeni za sprotno meritev razpoke iz podajnosti med preskusom. Pokazali smo, da je z uporabo aproksimacijskih funkcij mogoče veliko boljše simulirati zakon hitrosti rasti razpoke kot s Parisovo enačbo, ki pomeni linearizacijo dela tega zakona. To je pomembno za bolj realistično oceno trajnostne dobe konstrukcijskega elementa, izpostavljenega utrujanju.

Zahvala

Avtor se zahvaljuje Ministrstvu za šolstvo, znanost in šport RS za sofinanciranje raziskovalnega projekta v okviru katerega je nastal ta prispevek.

6 LITERATURA

[1] Evalds H. L., Wanhill R. J. H., Fracture mechanics, Edward Arnold in Delftse Uitgevers Maatschappij, Delft, 1985

[2] Lining W., Some Aspects of the Prediction of Fatigue Crack Paths. Mixed-Mode Fatigue and Fracture, ESIS 14 (Edited by P. Rossmanith and K. J. Miller), Mechanical Engineering Publications, London, 1993, 201-215

[3] Zhu J. Z., Zienkiewicz O. C., Hinton E., Wu J., A New Approach to the Development of Automatic Quadrilateral Mesh Generation. Int. J. Num. Meth. Eng., 32 (**1991**), 849-866

[4] Kovše I., Fatigue crack path prediction under the conditions of linear elastic fracture mechanics. Master's degree in Slovene) (No. 133), FGG, Ljubljana, 1996

[5] Hellen T. K., On the Method of Virtual Crack Extensions. Int. J. Num. Meth. Eng., 9 (**1975**) 187-207

[6] Xie M., Gerstle W. H., Rahulkumar P., Energy-Based Automatic Mixed-Mode Crack-Propagation Modeling. J. Eng. Mech. (ASCE), 121 (**1995**) 8, 914-923

[7] Kovše I., Fatigue crack in the elastic-plastic material. Ph. D. Thesis (in Slovene), Univerza v Ljubljani, FGG, 1998

[8] Bohte Z., Numerične metode. DZS, Ljubljana, 1978

[9] Smith F., Hooeppner D. W., Use of the Four Parameter Weibull Function for Fitting Fatigue and Compliance Calibration Data. Eng. Frac. Mech., 36 (**1990**) 1, 173-178